Smart Forestry

ORIGINAL RESEARCH

Open Access

https://doi.org/10.48130/smartfor-0025-0003

Smart Forestry **2026**, 1: e003

Thermal-index monitoring of water status in humid-region urban forests: a canopy-temperature-based approach

Qing Peng[1,2], Peng Yin[1], Xuemin Ye[1], Hongru Li[1], Xuan Liang[1,2], Zhaofei Tian[3], Yuexin Xiao[3], Xiangfen Cheng[4], Linqi Liu[1*], Kunshui Luo[1] and Wei Liu[2*]

[1] *Jiangxi Academy of Forestry, Jiangxi Nanchang Urban Ecosystem Research Station, Nanchang 330013, China*

[2] *Jiangxi Key Laboratory of Subtropical Forest Resources Cultivation, Jiangxi Agricultural University, Nanchang 330045, China*

[3] *Changsha Comprehensive Survey Center of Natural Resources, China Geological Survey, Huangshan Observation and Research Station for Land-water Resources, Changsha 410600, China*

[4] *Research Institute of Forestry, Chinese Academy of Forestry, Beijing 100091, China*

* Correspondence: liulinqi@caf.ac.cn (Liu L); w_liu08@163.com (Liu W)

Abstract

The plant water stress index (PWSI) based on canopy temperature has been widely employed to monitor crop water status in arid and semi-arid regions; however, its utility in forest ecosystems, particularly urban forests in humid regions experiencing pronounced seasonal drought, remains unexplored. This study selected the urban forest in Nanchang, China, as the research object. Through continuous observations of canopy temperature, meteorological variables, latent heat flux (*LE*), and canopy conductance (g_c) from July to October 2024, the study evaluated the performance of traditional water-status indicators: soil water content (*SWC*) and vapor pressure deficit (*VPD*), along with two canopy-temperature-derived thermal indices: the empirical PWSI ($PWSI_e$) and the theoretical PWSI ($PWSI_t$) for detecting water deficits in humid-region urban forests. Results showed that neither *SWC* nor *VPD* effectively tracked temporal variations in g_c or *LE* in this humid-region urban forest. Under well-watered conditions, non-water-stressed baselines (NWSB) were successfully established using either hourly daytime data or daytime mean data of the canopy-air temperature difference (*dT*) vs *VPD*. Nevertheless, owing to the combination of low atmospheric evaporative demand, weak sensitivity of *dT* to water deficit in woody vegetation, and strong radiative control of *dT*, $PWSI_e$ explained at most 29% of the variance in g_c and 31% of that in *LE*, irrespective of the NWSB formulation. In contrast, $PWSI_t$, derived from the canopy energy balance and the Penman-Monteith equation, exhibited good monitoring performance, with daytime mean $PWSI_t$ explaining 45% of the variance in g_c and 64% of that in *LE*. When canopy temperature was acquired using a northeasterly-oriented infrared camera, the optimal assessment window for ecosystem water status was 14:00–16:00 local time. Collectively, our findings demonstrate that $PWSI_t$ is a robust indicator for tracking water-status dynamics in humid-region urban forests, providing a reliable early-warning tool for detecting drought events in these ecosystems.

Citation: Peng Q, Yin P, Ye X, Li H, Liang X, et al. 2026. Thermal-index monitoring of water status in humid-region urban forests: a canopy-temperature-based approach. *Smart Forestry* 1: e003 https://doi.org/10.48130/smartfor-0025-0003

Introduction

Urban forests constitute a critical component of urban ecosystems, offering irreplaceable services such as carbon sequestration and oxygen release, microclimate regulation (cooling and humidification), air pollution mitigation, water quality improvement, and biodiversity conservation. These functions position urban forests as nature-based solutions for enhancing urban sustainability[1,2]. Global warming has markedly increased both the intensity and frequency of drought events, exerting substantial negative impacts on forest ecosystems[3]. However, most reports have concentrated on arid and semi-arid regions, whereas seasonal droughts in humid and sub-humid regions have received comparatively limited attention[4,5]. Studies indicate that forest ecosystems in humid regions are more sensitive to drought events than those in drier climates, exhibiting greater declines in forest productivity and elevated mortality rates[6]. This sensitivity is particularly pronounced in urban forest ecosystems, where rapid urbanization further exacerbates environmental problems—such as the urban-heat-island and urban-dry-island effects—thereby increasing the threats to forest health[7,8]. Timely and accurate monitoring of drought events in urban forests is an essential prerequisite for mitigating their adverse impacts. Such monitoring is critical for assessing ecosystem health, managing drought-related risks, and exerting the potential service functions of the ecosystem.

Due to the lack of effective indicators, tracking the daily water status of urban-forest ecosystems still faces many challenges[9]. It is well established that the earliest phase of drought is perceived by root systems, which respond by synthesizing and translocating abscisic acid (ABA) to the leaves. Elevated ABA concentrations in the apoplast of guard cells trigger rapid stomatal closure, thereby increasing diffusive resistance within the leaf and suppressing transpiration. Consequently, stomatal conductance (g_s) is considered the most sensitive indicator of plant water deficit and provides a mechanistic basis for the early detection of drought stress[10], whereas transpiration rate (T_r) quantifies the actual water consumption of the plant. Nevertheless, the acquisition of g_s and T_r demands professional equipment capable of only single-point measurements that are operationally challenging, labor-intensive, and often impractical in tall-stature trees[11,12]. Eddy covariance systems enable direct, automated determination of canopy conductance (g_c), evapotranspiration rate (ET_a), and its energy equivalent, latent heat flux (*LE*), at the ecosystem scale. However, their high cost, intensive maintenance, strict theoretical assumptions, and large source-area requirements limit their widespread deployment in urban forests[13]. Additionally, soil water content (*SWC*) and vapour pressure deficit (*VPD*), representing root-zone water supply and atmospheric evaporative demand, respectively, are both tightly coupled to vegetation growth and readily available, rendering them widely used indirect indicators of ecosystem water status. The IPCC Sixth Assessment Report, for instance, uses *SWC* and *VPD* to evaluate drought status in

forest ecosystems. However, studies indicate that low *SWC* is the principal determinant of drought risk in arid regions[14], whereas in humid regions, vegetation growth is more sensitive to changes in *VPD*[15].

Declines in g_s and T_r weaken the evaporative cooling process, resulting in elevated canopy temperature (T_c). Since T_c responds rapidly to stomatal behavior, it acts as a sensitive indicator of plant water deficit and can provide early warning of drought events. However, T_c is the result of the canopy energy balance and is influenced not only by plant water status but also by external environmental factors[16]. To overcome this defect, T_c or the canopy-air temperature difference (*dT*) must be normalized using thermal indices. Currently, commonly used thermal indices include the empirical plant water stress index ($PWSI_e$), the theoretical plant water stress index ($PWSI_t$), and the simplified plant water stress index ($PWSI_s$)[17]. These thermal indices are derived, respectively, from (1) the empirical negative relationship between *dT* and *VPD* under well-watered conditions, known as the non-water-stressed baseline (NWSB)[18]; (2) the canopy energy balance and the Penman-Monteith equation[19]; and (3) artificial or natural dry- and wet- reference surface temperatures[20]. Each approach defines the T_c or *dT* expected under non-water-stressed and non-transpiring conditions, thereby normalizing the observed T_c or *dT*. Due to the flexibility of mounting thermal infrared cameras on platforms such as towers, unmanned aerial vehicles (UAVs), or satellites, these thermal indices may be well-suited for daily monitoring of water status in patchily distributed urban forest ecosystems. However, to date, research on water status monitoring technology based on T_c has primarily focused on crops such as maize, wheat, cotton, rice, sunflower, soybean, and pumpkin[17,21–23].

Unlike annual crops, perennial woody plants generally adopt conservative water-use strategies to enhance stress tolerance[24,25]. This conservatism lowers transpirational cooling and weakens the T_c response to water deficit relative to annual crops. Additionally, the taller canopies of woody plants exhibit greater aerodynamic roughness for momentum and heat exchange, further weakening the expression of water-status differences in T_c[26]. Combined with the high variability of T_c caused by environmental influences, this may increase the difficulty of detecting drought in trees by thermal approaches. Moreover, the plant water stress index (PWSI) based on T_c was originally developed in the arid climate of Arizona, USA, where strong atmospheric evaporative demand amplifies transpirational forcing and facilitates the diagnosis of plant water status. However, in the low atmospheric evaporative demand of humid-region urban forests, the performance of PWSI in detecting the water deficit of perennial woody vegetation remains unclear and needs to be systematically evaluated. Additionally, the optimal monitoring window must be determined in order to facilitate future UAV-based urban forest water status diagnosis.

Nanchang, a major forest city in China, has a forest coverage of 21.27%. Although located in a humid climatic zone, the city is regularly subjected to seasonal drought events (summer and autumn droughts) that increasingly threaten the health of its urban forests. The extreme drought of 2022, for example, caused partial tree mortality across the region[27,28]. Against this background, continuous measurements of T_c, ecosystem-scale water fluxes, and key meteorological variables were conducted within Nanchang's urban forest. The objectives were: (1) to assess the suitability of traditional water-status indicators and canopy-temperature-based thermal indices for detecting water deficits in humid-region urban forests; (2) to elucidate the underlying reasons for their performance; and (3) to determine the optimal monitoring window.

Materials and methods

Site description

This study was conducted at the Jiangxi Nanchang Urban Ecosystem Observation and Research Station (28°45′ N, 115°46′ E, average altitude: 248.50 m), which is located 12.5 km from downtown Nanchang, China (Fig. 1). The study area has a subtropical humid monsoon climate, with an average annual temperature of 17.40 °C and an average annual precipitation of 1,848.70 mm. The soil type at the station is dominated by red earth and mountain yellow-red earth. Also, the main tree species in the plantation area include *Quercus acutissima*, *Sassafras tzumu*, *Cinnamomum camphora*, *Taxus chinensis var. mairei*, and *Magnolia denudata*, covering an area of approximately 133 ha, and having an average age of 60 years. The forest coverage rate at the site exceeds 90%, with an average tree height of 10 m and a maximum leaf area index (*LAI*) of 4.40. The understory is dominated by *Pyracantha fortuneana*, *Rhododendron simsii*, and *Litsea cubeba*. Although the canopy remains fully closed from April to October in the study area, frequent cloud cover and precipitation events during the earlier period (April–June) degrade the data quality of optical remote sensing. Consequently, analyses were restricted to sunny-day observations from July to October to evaluate the performance of traditional water-status indicators and the canopy-temperature-based PWSI in detecting water deficits within the urban forest ecosystem.

Fig. 1 The location of (a) the research site, (b) the illustration of flux tower, and (c) the thermal infrared imagery collected from the urban forest ecosystem.

Measurements

Canopy temperature

The canopy temperature of the Nanchang urban forest ecosystem was automatically monitored using a thermal infrared camera (FLIR A308, FLIR Systems Inc., Wilsonville, OR, USA) mounted on the flux tower platform at a height of 10 m above the canopy. Before the observation, the thermal infrared camera was calibrated with a commercial blackbody surface. The camera faced northeast with a sensor zenith angle of 45°. It uses an uncooled microbolometer to detect long-wave radiation between 7.50–13.00 μm and converts it to the temperature. Specifications include 320 × 240 pixel resolution, a 25° × 18.8° field of view, and an accuracy of ± 2 °C or ± 2% of the reading. The camera's emissivity was fixed at 0.96, and the images were collected every 5 min and transmitted to the server via a wireless transmission device. The canopy pixels were extracted from the thermal images using the temperature-threshold method. The temperature of the canopy pixels, derived through sky-temperature and path radiance calibration in the FLIR Tools software, was used to calculate T_c as their average temperature. Detailed processing steps can be found in Liu et al.[29].

Meteorological factors, ecosystem fluxes, and canopy structure parameters

Meteorological and eddy-covariance systems were installed on the 30 m flux tower. The meteorological observation system consisted of a temperature and humidity sensor (HMP155, Vaisala Inc., Vantaa, Finland), an anemometer (WindSonic, Gill Inc., Lymington, UK), a four-component net radiometer (CNR4, Kipp and Zonen Inc., Delft, Netherlands), and a rainfall gauge (TE525MM, Campbell Scientific Inc., Logan, UT, USA). Except for the four-component net radiometer, which was mounted 7 m above the canopy, all other sensors were installed at a height of 20 m. Additionally, four soil water content probes (CS655, Campbell Scientific Inc.) were inserted at depths of 10, 30, 50, and 70 cm, while two soil heat-flux plates (HFP01SC-L, Hukseflux Inc., Finland) were placed 5 cm below the surface at two points around the flux tower. All data were logged by a CR1000 data logger (Campbell Scientific Inc.) that stored 10 min averages. The eddy-covariance system, mounted at 30 m and comprising a three-dimensional sonic anemometer (CSAT3, Campbell Scientific Inc.) and a fast-response infrared gas analyzer (Li-7500A, Li-Cor Inc., Lincoln, NE, USA), continuously quantified water vapour exchange between the urban forest ecosystem and the atmosphere. Raw data were sampled at 10 Hz and recorded by a data logger (Model Li-7550, Li-Cor Inc.).

In addition, the plant canopy analyzer (LAI-2200C, Li-Cor Inc.) was used to measure the *LAI* of the urban forest ecosystem every 20 d, and linear interpolation was used to determine *LAI* values across the 20-d interval.

Data analysis

Flux data processing

Raw 10 Hz data were processed with EddyPro v7.0.7 (LI-COR Inc.) following standard quality-control steps: spike detection, 2-D coordinate rotation, Webb–Pearman–Leuning correction, block-averaging detrending, and friction velocity (u*) filtering (u* < 0.25 m·s^{-1}). Subsequently, 30-min averages of ecosystem latent heat fluxes (*LE*) were computed, and 75% of records passed quality control. Remaining gaps were filled using the marginal distribution sampling algorithm in the REddyProc R package (https://cran.r-project.org/package=REddyProc). The energy balance closure was 0.85. Detailed procedures follow Liu et al.[30] and Zhou et al.[31].

Sunny sky definition

In this study, the clear sky index (*CI*) was used to distinguish between cloudy and sunny days, and was calculated as follows, Gu et al.[32]:

$$CI = \frac{S_r}{S_e} \tag{1}$$

$$S_e = S_{sc} \times [1 + 0.033 \times \cos(360 t_d / 365)] \times \sin\varepsilon \tag{2}$$

$$\sin\varepsilon = \sin\varphi \times \sin\delta + \cos\varphi \times \cos\delta \times \cos\omega \tag{3}$$

where, S_r is the total radiation above the canopy (W m^{-2}), S_{sc} is the solar constant (1,367 W m^{-2}), S_e is the astronomical radiation (W m^{-2}), ε is the solar elevation angle, t_d is the Julian day, φ is the local latitude, ω is the time angle, δ is the declination of the sun. When the daily mean *CI* is greater than 0.5, the day is defined as sunny; otherwise, it is defined as cloudy[33].

Plant water stress index

The PWSI was calculated as follows, Idso et al.[18]:

$$\mathrm{PWSI} = \frac{dT - dT_{ll}}{dT_{ul} - dT_{ll}} \tag{4}$$

where, PWSI is the plant water stress index based on canopy temperature, dT is the measured canopy-air temperature difference (°C), dT_{ll} is the lower limit of dT, corresponding to the non-water-stressed condition, and dT_{ul} is the upper limit of dT, representing the non-transpiring condition (°C). Theoretically, the PWSI value ranges from zero to one, representing plant water status from well-watered to non-transpiring conditions.

Based on the different calculation methods for dT_{ll} and dT_{ul}, PWSI can be further categorized into PWSI$_e$, PWSI$_t$, and PWSI$_s$. Among these, PWSI$_s$ rely on manual observation of the reference surface temperature, which limits their application to automated monitoring of water status in forest ecosystems. Therefore, this study focuses only on the applicability of PWSI$_e$ and PWSI$_t$.

PWSI$_e$

The PWSI$_e$ was introduced by Idso et al.[18]. The dT_{ll} and dT_{ul} were determined by NWSB, defined as the negative linear relationship between dT_{ll} and *VPD*. Following Liu et al.[34] and Supplementary Fig. S1, this study identified eight well-watered days as those with g_c > 15 mm s^{-1} and established the NWSB from the corresponding dT_{ll} and *VPD* data.

Once the NWSB is determined, dT_{ll} and dT_{ul} are calculated as follows:

$$dT_{ll} = a \times VPD + b \tag{5}$$

$$VPD = 0.6108 \times e^{17.27 \times T_a/(T_a+237.3)} \times (1 - RH) \tag{6}$$

$$dT_{ul} = a \times VPG + b \tag{7}$$

$$VPG = 0.6108 \times e^{17.27 \times T_a/(T_a+237.3)} - 0.6108 \times e^{17.27 \times (T_a+b)/(T_a+b+237.3)} \tag{8}$$

where, the coefficients a and b represent the slope and intercept of NWSB, *VPD* is the vapor pressure difference (kPa), *VPG* is the vapor pressure gradient (kPa), T_a is the air temperature (°C), and *RH* is the air humidity (%).

PWSI$_t$

PWSI$_t$ estimates dT_{ll} and dT_{ul} through the canopy energy balance and the Penman–Monteith equation. Specifically, dT_{ll} is calculated by assuming the canopy resistance at potential transpiration, while dT_{ul} is derived by setting the canopy resistance to infinity. Detailed calculations follow Jackson et al.[19]:

$$dT_{ll} = \frac{r_a \times R_n}{\rho c_p} \cdot \frac{\gamma\left(1+\frac{r_{cp}}{r_a}\right)}{\Delta+\gamma\left(1+\frac{r_{cp}}{r_a}\right)} - \frac{VPD}{\Delta+\gamma\left(1+\frac{r_{cp}}{r_a}\right)} \quad (9)$$

$$dT_{ul} = \frac{r_a R_n}{\rho c_p} \quad (10)$$

where, R_n is the net radiation (W·m^{-2}), ρ is the air density (kg·m^{-3}), c_p is the heat capacity of the air (1,013 J·kg^{-1}·℃$^{-1}$), Δ is the slope of the saturation vapor pressure–temperature relationship (kPa·℃$^{-1}$), r_a is the aerodynamic resistance (s·m^{-1}), γ is the psychrometric constant (kPa·℃$^{-1}$), r_{cp} is the minimum canopy resistance (s·m^{-1}), and is calculated as follows Tong et al.[35]:

$$r_{cp} = \frac{r_{min}}{LAI_e} \quad (11)$$

$$LAI_e = \begin{cases} LAI & (LAI \le 2) \\ 2+\frac{LAI-2}{3} & (LAI > 2) \end{cases} \quad (12)$$

where, r_{min} is the minimum leaf stomatal resistance (90 s·m^{-1})[35], *LAI* is the leaf area index (m^2·m^{-2}), and LAI_e is the effective *LAI* (m^2·m^{-2}).

r_a was calculated using the semi-empirical equation presented by Thom & Oliver[36] and recommended by Jackson et al.[37]:

$$r_a = 4.72\left\{ln\left[\frac{(z-d)}{z_0}\right]\right\}^2/(1+0.54u) \quad (13)$$

where, z is the reference height (20 m), z_o and d are the roughness length (m) (z_o = *0.075 h*) and zero-plane displacement (m) (d = *0.66 h*)[30], respectively, u is the wind speed at the reference height (m·s^{-1}).

Canopy conductance

In this study, g_c was calculated based on the Penman-Monteith equation[38]:

$$g_c = \frac{LE \times \gamma}{\Delta \times r_a \times (R_n - G) + \rho C_p \times VPD - LE \times r_a \times (\Delta + \gamma)} \quad (14)$$

where, g_c is canopy conductance (mm·s^{-1}), G is the soil heat flux (W·m^{-2}), *LE* represents ecosystem latent heat flux (W·m^{-2}).

Statistical analysis

In this study, Pearson correlation analysis and partial correlation analysis were first employed to quantify the relationship among environmental factors, *dT*, and *LE*, and to identify the main driving factors of *dT*. According to the studies of García-Tejero et al.[39] and Bian et al.[40], g_c and *LE* served as indicators of the urban forest's actual water status, and the performance of *SWC*, *VPD*, and PWSI in tracking water status was evaluated by coefficients of determination (R^2) and significance levels (*p*-values). Among them, the *p*-values in this study were derived using t-statistics based on Newey-West adjusted standard errors. The above analyses were conducted using OriginPro 2024 (OriginLab Corporation, Northampton, MA, USA) and Python 3.11.0 with the statsmodels, scikit-learn, and NumPy libraries.

Results

Seasonal variations in environmental factors

The seasonal variations in the environmental parameters in the Nanchang urban forest ecosystem during the experimental period are shown in Fig. 2. R_n increased gradually in spring, peaked in summer, and declined thereafter, with pronounced fluctuations attributed to meteorological conditions. Particularly from April to June, frequent cloud cover and precipitation events led to relatively lower R_n values. Air temperature (T_a) followed the same trend, ranging from −4.52 °C in January to 33.64 °C in August. *VPD* was relatively high between July and August, with a peak value of 2.62 kPa. The wind speed (W_s) generally fluctuated around 2 m·s^{-1}, with a maximum value of 6.95 m·s^{-1}. Total rainfall in 2024 was 1,714.98 mm, less than the long-term mean. However, 62% of precipitation occurred from March to June, whereas July to October contributed only 19.7%, resulting in mean *SWC* (10, 30, 50, and 70 cm depths) of 0.17 m^3·m^{-3} in March–June and 0.15 m^3·m^{-3} in July–October, respectively. This seasonal imbalance indicates marked drought stress during the late growing season.

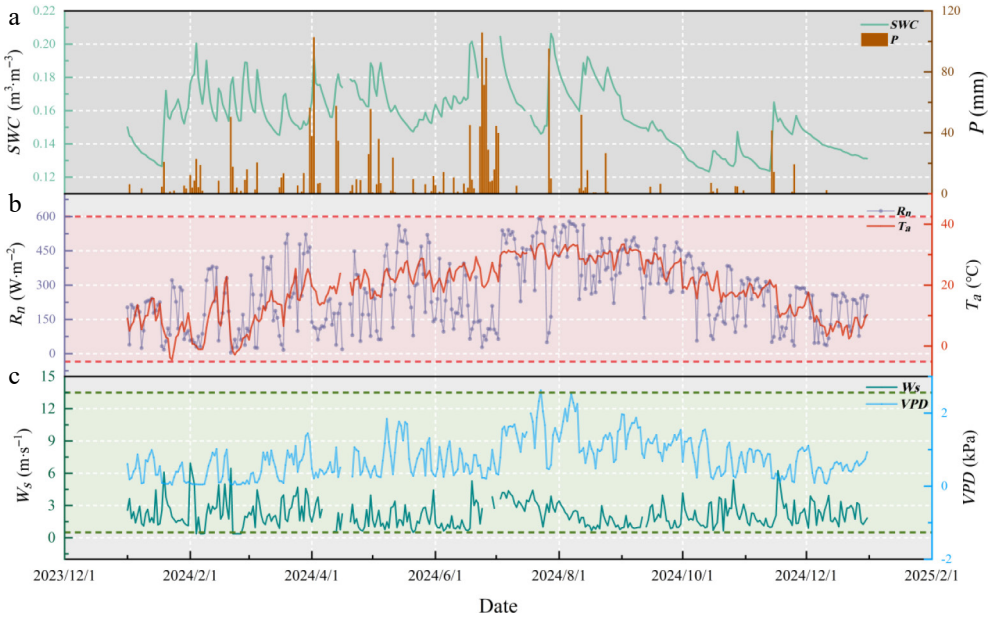

Fig. 2 Seasonal dynamics in (a) soil water content (*SWC*) and precipitation (*P*), (b) air temperature (T_a) and net radiation (R_n), (c) wind speed (W_s) and vapor pressure deficit (*VPD*) in the Nanchang urban forest ecosystem.

Relationship between canopy-air temperature difference and environmental factors

The *dT* in the Nanchang urban forest ecosystem was strongly influenced by environmental factors. Except for T_a, *VPD*, and *SWC*, all remaining variables were significantly correlated with the *dT* (p < 0.01). R_n was the dominant control factor, with a Pearson correlation coefficient (r) of 0.83, markedly higher than those of the other factors. *RH* and W_s followed, with coefficients of 0.14 and 0.13, respectively. In addition, *LE* and *dT* showed a significant positive correlation (r = 0.51, p < 0.01); with increasing heat dissipation, the *dT* of the urban forest ecosystem increased (Fig. 3).

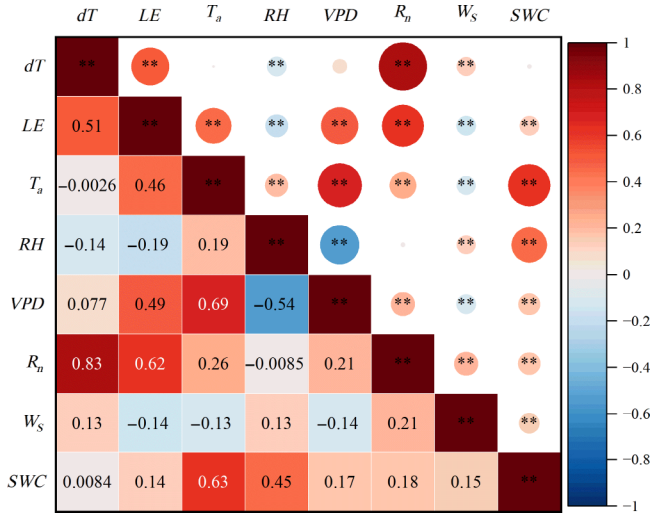

Fig. 3 Pearson's correlation coefficients among the canopy-air temperature difference (*dT*), latent heat flux (*LE*), and environmental variables under sunny days in the Nanchang urban forest ecosystem. ** represents p < 0.01; * represents p < 0.05.

Traditional indicators for urban forest water-status detection

During the study period, *LE* and g_c in the Nanchang urban forest ecosystem ranged from 100–450 W·m^{-2} and 4–20 mm·s^{-1}, respectively (Fig. 4). *LE* increased significantly with *SWC* (p < 0.01), yet *SWC* explained only 11% of the variance in *LE*. In contrast, *LE* did not exhibit a declining trend under elevated *VPD*; instead, a positive correlation was observed between the two variables. Although g_c tended to increase with higher *SWC* and lower *VPD*, neither *SWC* nor *VPD* was significantly correlated with g_c (p > 0.05) (Fig. 4). These results indicate that traditional water-status indicators fail to track variations in g_c or *LE* in humid-region urban forests and are insensitive to early drought events.

PWSI$_e$ for urban forest water-status detection

Establishment of the NWSB

The calculation of PWSI$_e$ relies on the relationship between dT_{II} and *VPD* to derive the NWSB. Figure 5 shows the result of NWSB, which was established by pooling dT_{II} and *VPD* data from all daytime

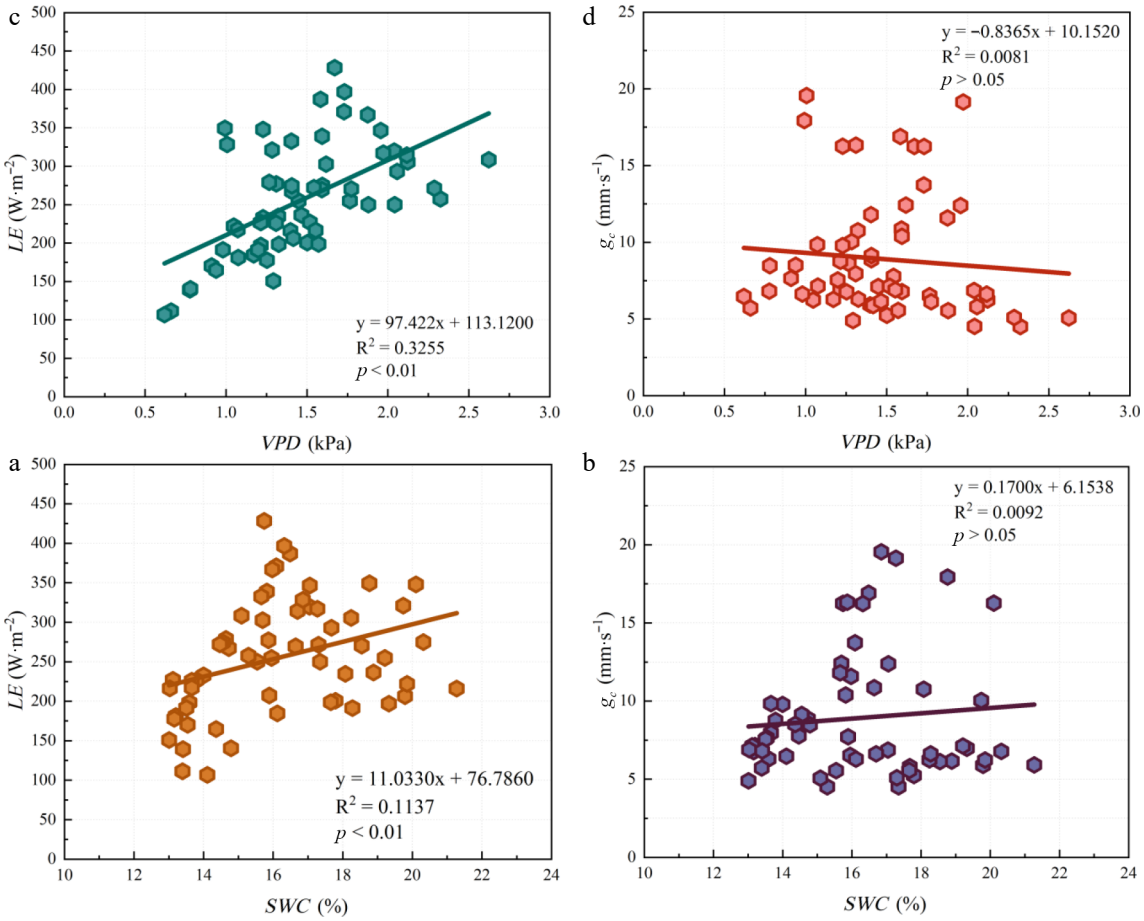

Fig. 4 Relationships among the soil water content (*SWC*), vapor pressure deficit (*VPD*), latent heat flux (*LE*), and canopy conductance (g_c). ** represents p < 0.01; * represents p < 0.05.

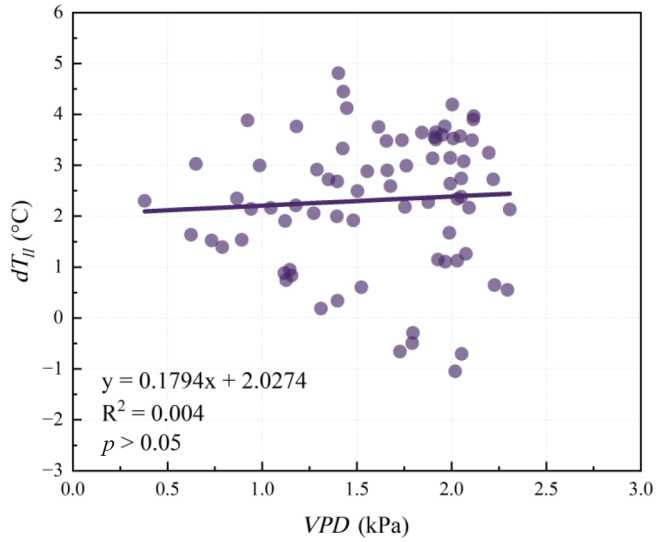

Fig. 5 Canopy-air temperature difference (dT_{ll}) vs vapour pressure deficit (*VPD*) under well-watered conditions (all daytime hours data on sunny days were pooled together). ** represents $p < 0.01$; * represents $p < 0.05$.

hours on sunny days throughout the study period. dT_{ll} ranged from −1.04 to 4.81 °C, and *VPD* from 0.38 to 2.31 kPa (the maximum hourly *VPD* recorded during the study period was 3.10 kPa). However, the data in Fig. 5 were too scattered to yield a reliable NWSB.

To accurately define the NWSB, the data were assessed in different ways. First, the NWSBs for the different hours of the daytime were determined (Table 1). Across all hours, dT_{ll} and *VPD* were negatively correlated, but the regression parameters varied markedly. Coefficients of determination (R^2) ranged from 0.08 to 0.87 and exhibited a clear diurnal pattern: R^2 followed a U-shaped trend, peaking at 0.84 in the early morning (08:00) and 0.87 in the late afternoon (17:00), and reaching a pronounced minimum of 0.08 at noon (12:00). An opposing trend was evident in the intercept values, which rose from 2.11 at 08:00 to 5.55 at 13:00 before declining to 2.37 at 17:00. By contrast, the slopes of the fitted relationships varied little, ranging from −0.54 to −1.02, except at 12:00, 14:00, and 17:00.

Subsequently, the NWSB was established using the daytime mean values of dT_{ll} and *VPD*. The results revealed a significant negative correlation between dT_{ll} and *VPD* ($p < 0.01$), with an R^2 of 0.86. The corresponding regression slope and intercept were −0.82 and 3.59, respectively (Table 1).

Relationships between the $PWSI_e$ and physiological variables

Table 2 summarizes the performance of hourly $PWSI_e$, based on NWSBs derived from different daytime periods, in detecting water-status changes in the Nanchang urban forest ecosystem. Between 09:00 and 11:00, $PWSI_e$ correlated negatively with g_c and *LE* ($p < 0.05$), yet the R^2 was relatively low: 0.15, 0.25, and 0.22 for g_c; 0.19, 0.29, and 0.31 for *LE*, respectively. Outside this narrow window, relationships deteriorated markedly; in some instances, $PWSI_e$ was positively correlated with g_c or *LE*, implying an anomalous increase in these variables under greater drought stress. These results indicate that hourly $PWSI_e$ derived from single-hour NWSBs is poorly suited for tracking the water status of humid-region urban forests and is subject to substantial uncertainty.

Figure 6 illustrates the performance of the daily $PWSI_e$, based on NWSB derived from daytime mean values of dT_{ll} and *VPD*, in detecting water-status changes in the urban forest ecosystem. Daily $PWSI_e$ fluctuated mainly between −0.4 and 0.5 (negative values account for 39% of the data), deviating markedly from the theoretical range of 0–1 for PWSI. Urban forest ecosystem *LE* was almost unaffected by daily $PWSI_e$ ($p > 0.05$). Although g_c decreased significantly as daily $PWSI_e$ increased ($p < 0.01$), the relationship was weak and highly scattered. These results indicate that daily $PWSI_e$ provides only limited insight into the water-status dynamics of humid-region urban forests.

Table 1. Fitted parameters for non-water-stressed baselines.

Time	Slope (°C·kPa^{-1})	Intercept (°C)	R^2
8:00	−0.9226	2.1068	0.8366**
9:00	−0.6772	2.7285	0.5622*
10:00	−0.6640	3.4301	0.2670
11:00	−0.5382	3.7108	0.1008
12:00	−0.2808	3.9867	0.0761
13:00	−0.8012	5.5463	0.5116*
14:00	−0.3989	4.3425	0.1421
15:00	−1.0205	4.4587	0.6430*
16:00	−0.8735	2.6552	0.2374
17:00	−1.5884	2.3692	0.8748**
8:00 – 17:00	−0.8227	3.5879	0.8633**

** represents $p < 0.01$; * represents $p < 0.05$ (same in all tables).

Table 2. Relationships between empirical plant water stress index ($PWSI_e$) and canopy conductance (g_c) and between $PWSI_e$ and latent heat flux (*LE*) at various times.

Time		Slope	Intercept	R^2
8:00	g_c	−0.0050	−0.0095	0.0036
	LE	0.0008	−0.2655	0.0278
9:00	g_c	−0.0289	0.5331	0.1609**
	LE	−0.0019	0.7765	0.2080**
10:00	g_c	−0.0595	0.9084	0.2507**
	LE	−0.0037	1.3350	0.2891**
11:00	g_c	−0.0729	1.2223	0.2154**
	LE	−0.0050	1.8831	0.3102**
12:00	g_c	−0.0781	1.0197	0.0282
	LE	−0.0078	2.3512	0.0838*
13:00	g_c	0.0087	−0.2427	0.0040
	LE	0.0020	−0.6967	0.0656
14:00	g_c	0.0253	−0.3908	0.0066
	LE	0.0055	−1.6110	0.0958*
15:00	g_c	0.0043	−0.1196	0.0013
	LE	0.0036	−1.0096	0.2621**
16:00	g_c	−0.0103	0.0991	0.0063
	LE	0.0031	−0.8023	0.1704**
17:00	g_c	−0.0086	0.0288	0.0090
	LE	0.0017	−0.4991	0.1077*

$PWSI_t$ for urban forest water-status detection

Relationships between the $PWSI_t$ and physiological variables

During the study period, the daytime mean $PWSI_t$ ($PWSI_{t\_day}$) from 08:00 to 17:00 derived by the theoretical method ranged between 0.15 and 0.60. As $PWSI_{t\_day}$ increased, g_c and *LE* declined progressively ($p < 0.01$) (Fig. 7). $PWSI_{t\_day}$ explained 45% and 64% of the observed variations in g_c and *LE*, respectively (Fig. 8). These results demonstrate that the theoretically derived $PWSI_t$ provides a robust means of tracking water-status changes in humid-region urban forests and enables early detection of ecosystem drought events.

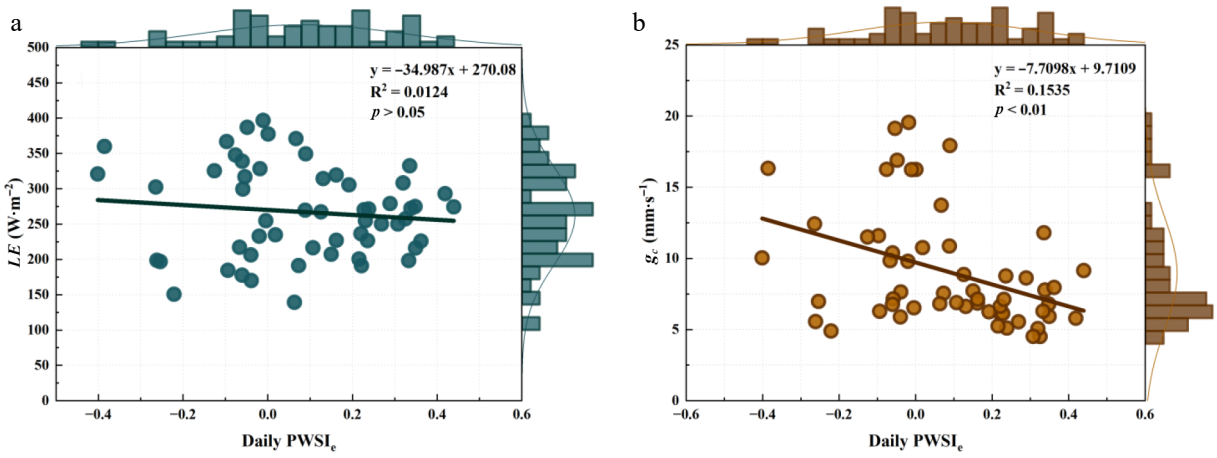

Fig. 6 Performance of the daily empirical plant water stress index ($PWSI_e$) in indicating urban forest ecosystem water status. ** represents $p < 0.01$; * represents $p < 0.05$.

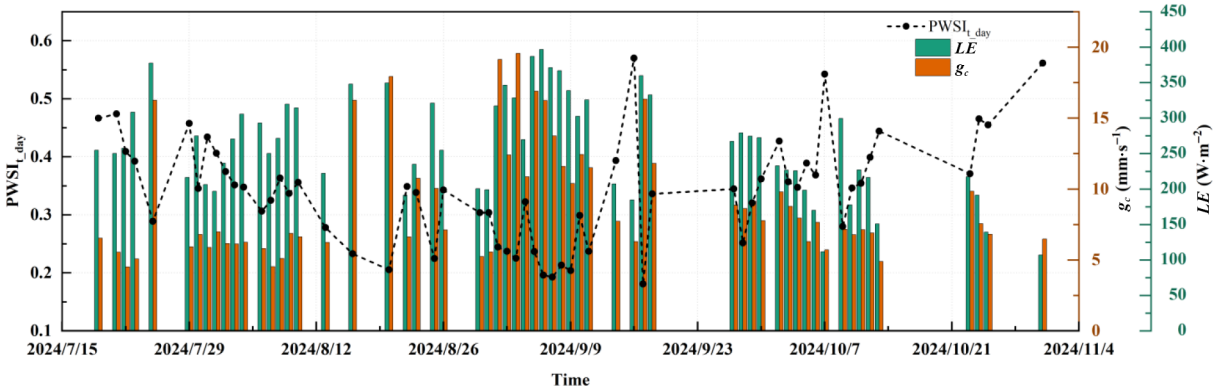

Fig. 7 Daily variations in the daytime mean theoretical plant water stress index ($PWSI_{t\_day}$), canopy conductance (g_c), and latent heat flux (*LE*) on sunny days from July to October 2024. ** represents $p < 0.01$; * represents $p < 0.05$.

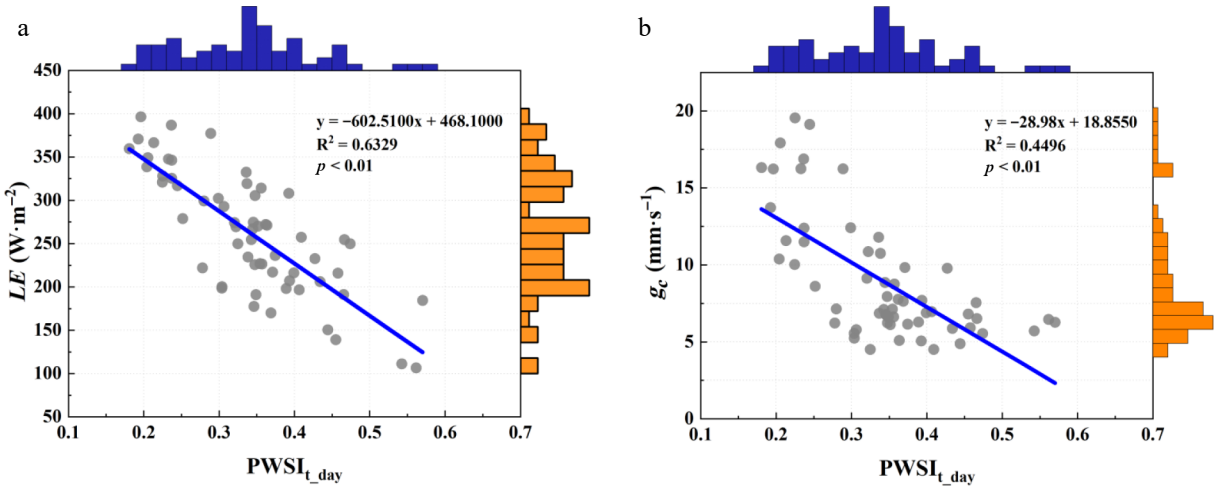

Fig. 8 Performance of the daytime mean theoretical plant water stress index ($PWSI_{t\_day}$) in indicating urban forest ecosystem water status. ** represents $p < 0.01$; * represents $p < 0.05$.

The optimal timing for detecting the water status of the urban forest ecosystem

Identifying the optimal monitoring window is essential for future mapping of water-deficit conditions across urban forests using unmanned aerial platforms. Table 3 summarizes the relationships between hourly $PWSI_t$ and g_c and *LE* at various times. Across all times, increasing $PWSI_t$ corresponded to monotonic declines in both g_c and *LE*. However, performance was poorest between 08:00 and 13:00, when $PWSI_t$ explained at most 23% of the variance in g_c and 11% of that in *LE*. In contrast, $PWSI_t$ performed markedly better from 14:00 to 16:00. At 14:00, it accounted for 45% of the variability in g_c; at 15:00 and 16:00, it explained 49% and 54% of the variability in *LE*, respectively. These findings suggest that $PWSI_t$ derived between 14:00 and 16:00 best represents the daily water status of the urban forest ecosystem in the study area.

Table 3. Relationships between theoretical plant water stress index ($PWSI_t$) and canopy conductance (g_c) and between $PWSI_t$ and latent heat flux (*LE*) at various times.

Time		Slope	Intercept	R^2
8:00	g_c	−0.0100	0.2976	0.0320
	LE	−0.0008	0.4058	0.0556
9:00	g_c	−0.0126	0.2601	0.1315**
	LE	−0.0006	0.3169	0.1051*
10:00	g_c	−0.0131	0.2804	0.1995**
	LE	−0.0005	0.3061	0.1060*
11:00	g_c	−0.0081	0.2735	0.1093**
	LE	−0.0002	0.2489	0.0171
12:00	g_c	−0.0129	0.3831	0.2121**
	LE	−0.0003	0.3433	0.0327
13:00	g_c	−0.0131	0.4530	0.2288**
	LE	−0.0005	0.4706	0.1084*
14:00	g_c	−0.0215	0.6037	0.4517**
	LE	−0.0010	0.6855	0.3262**
15:00	g_c	−0.0250	0.7123	0.3034**
	LE	−0.0018	0.9660	0.4931**
16:00	g_c	−0.0221	0.7961	0.1857**
	LE	−0.0022	1.1638	0.5400**
17:00	g_c	−0.0123	0.9101	0.0309
	LE	−0.0025	1.4561	0.3940**

Discussion

Limitations of conventional and dT proxies in humid-region urban forests

As global warming intensifies, seasonal drought events, such as summer and autumn droughts, have become more frequent across humid southern China, posing significant threats to the health of urban forest ecosystems. Currently, the monitoring and assessment of drought in forest ecosystems remain challenging, primarily due to the lack of effective indicators for water deficit[9]. *SWC* and *VPD* are commonly employed as indirect indicators of ecosystem water status and are used to assess ecosystem responses and adaptation strategies to drought. However, results reveal that neither *SWC* nor *VPD* is strongly associated with g_c or *LE* (Fig. 4). This may be attributed to the fact that g_c and *LE* are heavily influenced by external environmental conditions[41], particularly solar radiation, which serves as a key driver of *LE* (Fig. 3). Furthermore, plant water status is jointly regulated by soil water availability and atmospheric evaporative demand; thus, relying solely on a single indicator fails to accurately capture the water status of urban forests[35,42,43]. This further illustrates that traditional water status indicators are inadequate for the early detection of drought events in humid-region urban forests.

dT is strongly influenced by environmental factors, which compromise its use for accurate plant water-status monitoring. In this study, *dT* did not decrease with increasing W_s; instead, the two variables were significantly positively correlated (Fig. 3). Current studies on the influence of W_s on *dT* remain controversial. For example, Deng et al.[44] found that *dT* and W_s were negatively correlated when investigating the relationship between *dT* and environmental factors in a rubber plantation. In contrast, Kim et al.[45] reported that the *dT* of noble fir increased progressively with rising W_s. This conflicting result may be attributable to wind gustiness. According to the heat-transfer theory, W_s affects *dT* through convective heat exchange between the canopy and the air[46]. When the energy of convective heat exchange is held constant, higher W_s should reduce *dT*. However, this energy varies substantially under different environmental conditions, leading to the inconsistent *dT* responses to W_s reported across studies. Additionally, this study found that *dT* in the humid-region urban forest was primarily driven by solar radiation (Fig. 3), consistent with the observations of Kim et al.[47]. After removing the influence of radiation, the strong positive correlation between *dT* and *LE* disappeared, indicating that R_n was the primary reason why *dT* did not decrease despite increased heat dissipation (Fig. 3 and Supplementary Fig. S2). This pattern reflects the characteristics of humid-region forests, where the warming effect of R_n on *dT* is greater than the cooling effect of *LE* on *dT* due to the weak atmospheric evaporative demand; consequently, increased heat dissipation does not lead to a decline in *dT*[30]. This radiative dominance presents a significant challenge for drought detection based on *dT* in humid regions.

NWSB optimization and $PWSI_e$ limitations in humid-region urban forests

Developing thermal indices is an effective way to reduce environmental interference in *dT* and thereby improve the accuracy of plant water-deficit monitoring. Owing to its few-variable requirements (only T_a, *RH*, and T_c), computational simplicity, practical robustness, and ease of deployment, $PWSI_e$ is often prioritized for monitoring plant water status. In $PWSI_e$, both dT_{ll} and dT_{ul} are derived from the NWSB; consequently, establishing an appropriate NWSB is critical for using $PWSI_e$ to track plant water status accurately. Idso et al.[18] suggested that, for crops, a robust NWSB can be established using dT_{ll} and *VPD* data collected 2–3 h after sunrise until 2–3 h before sunset. In contrast, the study of a humid-region urban forest shows that when hourly dT_{ll} and *VPD* data from the entire daytime period on sunny days are pooled together, the relationship collapses: the data are highly scattered and no significant correlation exists (Fig. 5). This result agrees with findings in olive orchards in Seville[48] and grapefruit trees in Molina de Segura[49]. The primary reason is that, in the study area, *dT* is governed by solar radiation rather than by *VPD* (Fig. 3).

By applying the time-segment regression method, the influence of diurnal solar radiation variation on the relationship between dT_{ll} and *VPD* in woody plants can be mitigated, thereby enhancing the reliability of NWSB (Table 1). Similar improvements have been documented for perennial woody plants such as pistachio, grapefruit, grapevine, and olive[48–51]. According to the theoretical equation proposed by Jackson et al.[19], the NWSB intercept is governed by aerodynamic resistance and R_n, whereas the slope depends solely on aerodynamic resistance. Consequently, the intercept is expected to increase with rising radiation or decreasing wind speed, while the slope should increase as wind speed declines. This expectation agrees with the findings: due to diurnal solar radiation variation and the gustiness of wind, the intercept of the urban-forest NWSB exhibited a pronounced diurnal pattern—an inverted U-shape that mirrors solar radiation—whereas the slope varied little, averaging −0.82 (Table 1), close to the value of −0.74 reported by Liu et al.[34] for *Acacia pycnantha*. Comparable results have also been reported by Testi et al.[50] and Egea et al.[48] in pistachio and olive orchards. Furthermore, it was observed that the R^2 of the NWSB derived from daytime mean dT_{ll} and *VPD* data was higher than that of most single-hour NWSBs (Table 1). This finding supports the results of Osroosh et al.[52] in an apple orchard, who demonstrated that daytime mean NWSB can mitigate the interference of environmental factors.

Although the NWSB can be established through time-segment regression or by using daytime mean dT_{ll} and *VPD* data, this study shows that $PWSI_e$ derived from either single-hour or daytime mean NWSB is a weak indicator for monitoring water status in humid-

region urban forests (Table 2, Fig. 6). This outcome conflicts with the findings of Alghory & Yazar[53], who successfully employed $PWSI_e$ to assess wheat water status under humid-season conditions; however, it is consistent with the results reported by Testi et al.[50] for pistachio. *dT* depends on the energy balance and is regulated by R_n and *LE*. The principle of $PWSI_e$ for monitoring plant water status is that *VPD* drives transpiration, enhancing evaporative cooling and thereby lowering *dT*. The magnitude of *dT* reduction varies across different plant water conditions. However, compared with crops, woody plants have lower transpirational cooling capacity, making *dT* less sensitive to water deficits. Previous studies report that NWSB slopes for crops such as sesame, maize, pumpkin, wheat and soybean are −2.70, −1.97, −3.09, −2.02, and −2.19 °C·kPa^{-1}, respectively, whereas values for perennial woody plants—orange, mandarin, olive, peach and pistachio—are only −0.38, −0.50, −0.35, −1.70, and −1.35 °C·kPa^{-1}[23,51,54–58]. This reduced sensitivity means that rising atmospheric evaporative demand causes smaller *dT* reductions in woody plants than in crops. Consequently, the resulting NWSB slopes are shallower, and the temperature differences between dT_{ll} and dT_{ul} required for $PWSI_e$ calculations are narrower. Coupled with the weakened driving effect of *VPD* on plant transpiration in humid-region urban forests, this indirectly amplifies the disturbance of *dT* by environmental fluctuations, particularly solar radiation (Fig. 3). However, the NWSB does not account for radiation interference. As a result, the measured *dT* frequently falls outside the dT_{ll}–dT_{ul} range, generating abnormal $PWSI_e$ values (Fig. 6). This leads to a deterioration in reliability and an inevitable worsening of the signal-to-noise ratio. Testi et al.[50] further noted that, even when a well-defined NWSB is available, $PWSI_e$ becomes ineffective for monitoring pistachio water status under *VPD* < 2 kPa. Liu et al.[30] observed similar limitations in a *Quercus variabilis* plantation and recommended integrating multiple meteorological variables and canopy-structural parameters through data-driven approaches to calculate dT_{ll} and $PWSI_e$.

$PWSI_t$ enables early drought detection in humid urban forests

By explicitly incorporating solar radiation and W_s-dependent aerodynamic resistance into the calculation of dT_{ll} and dT_{ul}, $PWSI_t$ overcomes the challenge in humid-region forests—where the warming effect of R_n on *dT* outweighs the cooling effect of *LE* on *dT*—and thereby accurately tracks variations in g_c and *LE* (Figs 7, 8). Comparable findings have been reported by Ben-Gal et al.[59], Han et al.[60], and Liu et al.[30]. This confirms that $PWSI_t$ is suitable for the early detection of water deficits and the timely identification of drought events in urban forests. Previous studies often regard midday as the optimal window for PWSI-based water-status detection, as high transpiration rates and pronounced evaporative cooling amplify differences in *dT* and g_c under different water conditions[34,51]. In contrast, these results indicate that $PWSI_t$ performs best between 14:00 and 16:00 (Table 3), a finding consistent with the observations of García-Tejero et al.[39] in a vineyard. Such a difference may be traced to the orientation of the infrared camera. Currently, some studies use a nadir view, which maximizes incident radiation at noon but covers only a small observation area. Owing to site constraints, the study's camera faced northeast; direct solar irradiation of the canopy in this direction peaks between 14:00 and 16:00 (the distributions of solar zenith and solar azimuth angles range from 18° to 67° and from 241° to 262°, respectively), which yields the most pronounced thermal contrast for drought detection. Future work should systematically evaluate how camera orientation influences $PWSI_t$ performance and the optimal detection window, thereby laying the groundwork for PWSI deployment on unmanned aerial platforms.

The early-detection capability of $PWSI_t$ can translate trees' physiological responses to warming and drought into a quantifiable assessment of adaptive potential. Beyond deepening the understanding of stress-resistance mechanisms, this indicator directly serves climate-smart forestry management: by identifying 'vulnerable' and 'robust' individuals, it lays a critical foundation for building more resilient and adaptable urban forests of the future.

Conclusions

SWC and *VPD* alone are ineffective for detecting early drought events in humid-region urban forests. Within humid-region forests, *dT* is strongly controlled by solar radiation; combined with the region's low atmospheric evaporative demand and the comparatively weak sensitivity of *dT* to water deficit in woody plants, this severely limits the ability of the $PWSI_e$ to provide both early detection and continuous tracking of water deficits. By contrast, the $PWSI_t$ incorporates meteorological and resistance parameters, thereby suppressing solar-radiation-induced noise in *dT* and reliably reflecting variations in g_c and *LE*, offering a robust method for early detection of drought events in urban forests. When the camera faces northeast, $PWSI_t$ values obtained between 14:00 and 16:00 are recommended for assessing forest water status. Future research should systematically evaluate how sensor deployment strategies affect the accuracy of PWSI monitoring.

Author contributions

The authors confirm contributions to the paper as follows: study conception and design: Liu L, Liu W; methodology: Yin P, Peng Q; software: Peng Q, Tian Z, Liang X; validation: Ye X, Li H, Liu L; visualization: Xiao Y, Cheng X, Luo K; draft manuscript preparation: Liu L; writing—review and editing: Liu L, Cheng X, Yin P; funding acquisition: Liu L. All authors reviewed the results and approved the final version of the manuscript.

Data availability

The datasets generated during and/or analyzed during the current study are not publicly available due to the author is preparing to build a comprehensive database, but are available from the corresponding author upon reasonable request.

Acknowledgements

This work was supported by the Basic Research and Talent Research Project of Jiangxi Academy of Forestry (Grant Nos 2024520801, 2025520802), the Youth Fund Project of Natural Science Foundation of Jiangxi Province (Grant No. 20242BAB20260), the Youth Science and Technology Project of Jiangxi (Grant No. 20244BCE52288), and the Open Research Project of the Ecological Conservation Redline Field Scientific Observation and Research Station of the Poyang Lake Basin, Ministry of Natural Resources (Grant No. JXZSZ2025004).

Conflict of interest

The authors declare that there is no conflict of interest.

Dates

Received 29 August 2025; Revised 21 December 2025; Accepted 25 December 2025; Published online 28 January 2026

References

[1] Uniyal S, Purohit S, Chaurasia K, Rao SS, Amminedu E. 2022. Quantification of carbon sequestration by urban forest using Landsat 8 OLI and machine learning algorithms in Jodhpur, India. *Urban Forestry & Urban Greening* 67:127445

[2] Yao N, Konijnendijk van den Bosch CC, Yang J, Devisscher T, Wirtz Z, et al. 2019. Beijing's 50 million new urban trees: Strategic governance for large-scale urban afforestation. *Urban Forestry & Urban Greening* 44:126392

[3] Choat B, Jansen S, Brodribb TJ, Cochard H, Delzon S, et al. 2012. Global convergence in the vulnerability of forests to drought. *Nature* 491:752–755

[4] Asner GP, Brodrick PG, Anderson CB, Vaughn N, Knapp DE, et al. 2016. Progressive forest canopy water loss during the 2012–2015 California drought. *Proceedings of the National Academy of Sciences of the United States of America* 113(2):E249–E255

[5] Goulden ML, Bales RC. 2019. California forest die-off linked to multi-year deep soil drying in 2012–2015 drought. *Nature Geoscience* 12(8):632–637

[6] Vicente-Serrano SM, Gouveia C, Camarero JJ, Beguería S, Trigo R, et al. 2013. Response of vegetation to drought time-scales across global land biomes. *Proceedings of the National Academy of Sciences of the United States of America* 110(1):52–57

[7] Huang X, Hao L, Sun G, Yang ZL, Li W, et al. 2022. Urbanization aggravates effects of global warming on local atmospheric drying. *Geophysical Research Letters* 49(2):e2021GL095709

[8] Sjöman H, Hirons AD, Bassuk NL. 2015. Urban forest resilience through tree selection—variation in drought tolerance in Acer. *Urban Forestry & Urban Greening* 14(4):858–865

[9] Cui J, Chen A, Huntingford C, Piao S. 2024. Integrating ecosystem water demands into drought monitoring and assessment under climate change. *Nature Water* 2(3):215–218

[10] Jones HG. 2004. Irrigation scheduling: advantages and pitfalls of plant-based methods. *Journal of Experimental Botany* 55(407):2427–36

[11] Ballester C, Jiménez-Bello MA, Castel JR, Intrigliolo DS. 2013. Usefulness of thermography for plant water stress detection in citrus and persimmon trees. *Agricultural and Forest Meteorology* 168:120–129

[12] Gontia NK, Tiwari KN. 2008. Development of crop water stress index of wheat crop for scheduling irrigation using infrared thermometry. *Agricultural Water Management* 95(10):1144–1152

[13] Shi TT, Guan DX, Wu JB, Wang AZ, Jin CJ, et al. 2008. Comparison of methods for estimating evapotranspiration rate of dry forest canopy: eddy covariance, Bowen ratio energy balance, and penman-monteith equation. *Journal of Geophysical Research* 113(D19):2008JD010174

[14] Diffenbaugh NS, Swain DL, Touma D. 2015. Anthropogenic warming has increased drought risk in California. *Proceedings of the National Academy of Sciences of the United States of America* 112(13):3931–3936

[15] Wang S, Fu B, Wei F, Piao S, Maestre FT, et al. 2023. Drylands contribute disproportionately to observed global productivity increases. *Science Bulletin* 68(2):224–232

[16] Agam N, Cohen Y, Alchanatis V, Ben-Gal A. 2013. How sensitive is the CWSI to changes in solar radiation? *International Journal of Remote Sensing* 34(17):6109–6120

[17] Katimbo A, Rudnick DR, DeJonge KC, Lo TH, Qiao X, et al. 2022. Crop water stress index computation approaches and their sensitivity to soil water dynamics. *Agricultural Water Management* 266:107575

[18] Idso SB, Jackson RD, Pinter PJ, Reginato RJ, Hatfield JL. 1981. Normalizing the stress-degree-day parameter for environmental variability. *Agricultural Meteorology* 24:45–55

[19] Jackson RD, Idso SB, Reginato RJ, Pinter PJ Jr. 1981. Canopy temperature as a crop water stress indicator. *Water Resources Research* 17(4):1133–1138

[20] Jones HG. 1999. Use of thermography for quantitative studies of spatial and temporal variation of stomatal conductance over leaf surfaces. *Plant, Cell & Environment* 22(9):1043–1055

[21] Sánchez-Piñero M, Martín-Palomo MJ, Andreu L, Moriana A, Corell M. 2022. Evaluation of a simplified methodology to estimate the CWSI in olive orchards. *Agricultural Water Management* 269:107729

[22] Zhang L, Zhang H, Zhu Q, Niu Y. 2023. Further investigating the performance of crop water stress index for maize from baseline fluctuation, effects of environmental factors, and variation of critical value. *Agricultural Water Management* 285:108349

[23] Zhang Q, Yang X, Liu C, Yang N, Yu G, et al. 2024. Monitoring soil moisture in winter wheat with crop water stress index based on canopy-air temperature time lag effect. *International Journal of Biometeorology* 68(4):647–659

[24] Liu P, Tong X, Meng P, Zhang J, Li J, et al. 2022. b. *Biophysical controls on water use efficiency of six plantations under different sky conditions. Agricultural and Forest Meteorology* 320:108938

[25] Pan SA. 2022. *Variation of hydraulic conductivity at altitude and related morphological and physiological characteristics of Faxon fir*. Thesis (in Chinese). Beijing Forestry University, China

[26] Maes WH, Steppe K. 2012. Estimating evapotranspiration and drought stress with ground-based thermal remote sensing in agriculture: a review. *Journal of Experimental Botany* 63(13):4671–4712

[27] Chen Q, Liu Y, Fu X, Hou Y, Hui J, et al. 2025. Water-use strategies of Chinese fir to simulated precipitation change in a subtropical region. *Forestry: An International Journal of Forest Research* 00:cpaf041

[28] Wang X, Guo H, Bao YMD, Zhou GY, Chen YH, et al. 2025. Damaged characteristics and influencing factors of cunninghamia lanceolata mixed plantations in subtropics under extreme drought conditions. *Scientia Silvae Sinica* 61(5):12–22 (in Chinese)

[29] Liu L, Xie Y, Gao X, Cheng X, Huang H, et al. 2021. A new Threshold-Based method for extracting canopy temperature from thermal infrared images of Cork oak plantations. *Remote Sensing* 13(24):5028

[30] Liu L, Gao X, Ren C, Cheng X, Zhou Y, et al. 2022. Applicability of the crop water stress index based on canopy–air temperature differences for monitoring water status in a cork oak plantation, northern China. *Agricultural and Forest Meteorology* 327:109226

[31] Zhou Y, Zhang J, Yin C, Huang H, Sun S, et al. 2022. Empirical analysis of the influences of meteorological factors on the interannual variations in carbon fluxes of a Quercus variabilis plantation. *Agricultural and Forest Meteorology* 326:109190

[32] Gu LH, Fuentes JD, Shugart HH, Staebler RM, Black TA. 1999. Responses of net ecosystem exchanges of carbon dioxide to changes in cloudiness: Results from two North American deciduous forests. *Journal Of Geophysical Research-atmospheres* 104(D24):31421–31434

[33] Li Z, Zhang Q, Li J, Yang X, Wu Y, et al. 2020. Solar-induced chlorophyll fluorescence and its link to canopy photosynthesis in maize from continuous ground measurements. *Remote Sensing of Environment* 236:111420

[34] Liu N, Deng Z, Wang H, Luo Z, Gutiérrez-Jurado HA, et al. 2020. Thermal remote sensing of plant water stress in natural ecosystems. *Forest Ecology and Management* 476:118433

[35] Tong X, Mu Y, Zhang J, Meng P, Li J. 2019. Water stress controls on carbon flux and water use efficiency in a warm-temperate mixed plantation. *Journal of Hydrology* 571:669–678

[36] Thom AS, Oliver HR. 1977. On Penman's equation for estimating regional evaporation. *Quarterly Journal of the Royal Meteorological Society* 103(436):345–357

[37] Jackson RD, Kustas WP, Choudhury BJ. 1988. A reexamination of the crop water stress index. *Irrigation science* 9(4):309–317

[38] Monteith JL, Reifsnyder WE. 1974. Principles of Environmental Physics. *Physics Today* 27(3):51–52

[39] García-Tejero IF, Costa JM, Egipto R, Durán-Zuazo VH, Lima RSN, et al. 2016. Thermal data to monitor crop-water status in irrigated Mediterranean viticulture. *Agricultural Water Management* 176:80–90

[40] Bian J, Zhang Z, Chen J, Chen H, Cui C, et al. 2019. Simplified evaluation of cotton water stress using high resolution unmanned aerial vehicle thermal imagery. *Remote Sensing* 11(3):267

[41] Jarvis PG, McNaughton KG. 1986. Stomatal control of transpiration: scaling up from leaf to region. *Advances in Ecological Research* 15:1–49

[42] Rigden AJ, Mueller ND, Holbrook NM, Pillai N, Huybers P. 2020. Combined influence of soil moisture and atmospheric evaporative demand is important for accurately predicting US maize yields. *Nature Food* 1(2):127–133

[43] Wilson TG, Kustas WP, Alfieri JG, Anderson MC, Gao F, et al. 2020. Relationships between soil water content, evapotranspiration, and irrigation measurements in a California drip-irrigated Pinot noir vineyard. *Agricultural Water Management* 237:106186

[44] Deng C, Wu ZX, Tan ZH, Liao LG, Cui YB, et al. 2020. Variations of canopy temperature in a rubber plantation in Western Hainan Island and their relations with micrometeorological factors. *Chinese Journal of Tropical Crops* 41(7):1490−1497 (in Chinese)

[45] Kim Y, Still CJ, Roberts DA, Goulden ML. 2018. Thermal infrared imaging of conifer leaf temperatures: Comparison to thermocouple measurements and assessment of environmental influences. *Agricultural and Forest Meteorology* 248:361−371

[46] Gates DM. 1980. *Biophysical Ecology*. New York: Springer-Verleg. pp. 15

[47] Kim Y, Still CJ, Hanson CV, Kwon H, Greer BT, et al. 2016. Canopy skin temperature variations in relation to climate, soil temperature, and carbon flux at a ponderosa pine forest in central Oregon. *Agricultural and Forest Meteorology* 226−227:161−173

[48] Egea G, Padilla-Díaz CM, Martinez-Guanter J, Fernández JE, Pérez-Ruiz M. 2017. Assessing a crop water stress index derived from aerial thermal imaging and infrared thermometry in super-high density olive orchards. *Agricultural Water Management* 187:210−221

[49] Romero-Trigueros C, Bayona Gambín JM, Nortes Tortosa PA, Alarcón Cabañero JJ, Nicolás Nicolás E. 2019. Determination of crop water stress index by infrared thermometry in grapefruit trees irrigated with saline reclaimed water combined with deficit irrigation. *Remote Sensing* 11(7):757−780

[50] Testi L, Goldhamer DA, Iniesta F, Salinas M. 2008. Crop water stress index is a sensitive water stress indicator in pistachio trees. *Irrigation Science* 26(5):395−405

[51] Bellvert J, Zarco-Tejada PJ, Girona J, Fereres E. 2014. Mapping crop water stress index in a 'Pinot-noir' vineyard: comparing ground measurements with thermal remote sensing imagery from an unmanned aerial vehicle. *Precision Agriculture* 15(4):361−376

[52] Osroosh Y, Peters RT, Campbell CS. 2016. Daylight crop water stress index for continuous monitoring of water status in apple trees. *Irrigation Science* 34(3):209−219

[53] Alghory A, Yazar A. 2019. Evaluation of crop water stress index and leaf water potential for deficit irrigation management of sprinkler-irrigated wheat. *Irrigation Science* 37(1):61−77

[54] Anda A, Simon B, Soós G, Teixeira da Silva JA, Kucserka T. 2019. Crop-water relation and production of two soybean varieties under different water supplies. *Theoretical and Applied Climatology* 137(1-2):1515−1528

[55] Bellvert J, Marsal J, Girona J, Gonzalez-Dugo V, Fereres E, et al. 2016. Airborne thermal imagery to detect the seasonal evolution of crop water status in peach, nectarine and saturn peach orchards. *Remote Sensing* 8(1):39

[56] Berni JAJ, Zarco-Tejada PJ, Sepulcre-Cantó G, Fereres E, Villalobos F. 2009. Mapping canopy conductance and CWSI in olive orchards using high resolution thermal remote sensing imagery. *Remote Sensing of Environment* 113(11):2380−2388

[57] Gonzalez-Dugo V, Zarco-Tejada PJ. 2024. Assessing the impact of measurement errors in the calculation of CWSI for characterizing the water status of several crop species. *Irrigation Science* 42(3):431−443

[58] Khorsandi A, Hemmat A, Ahmad Mireei S, Amirfattahi R, Ehsanzadeh P. 2018. Plant temperature-based indices using infrared thermography for detecting water status in sesame under greenhouse conditions. *Agricultural Water Management* 204:222−233

[59] Ben-Gal A, Agam N, Alchanatis V, Cohen Y, Yermiyahu U, et al. 2009. Evaluating water stress in irrigated olives: correlation of soil water status, tree water status, and thermal imagery. *Irrigation Science* 27(5):367−376

[60] Han M, Zhang H, DeJonge KC, Comas LH, Gleason S. 2018. Comparison of three crop water stress index models with sap flow measurements in maize. *Agricultural Water Management* 203:366−375